

The 43GHz SiO maser in the circumstellar envelope of the AGB star R Cassiopeiae

K. A. Assaf¹, P. J. Diamond^{1,2}, A. M. S. Richards¹ and M. D. Gray¹

¹*JBCA, Alan Turing Building, School of Physics and Astronomy, The University of Manchester, Oxford Road, Manchester, M13 9PL, UK*

²*CSIRO Astronomy and Space Sciences, PO Box 76, Epping, NSW 1710, Australia*

25 October 2018

ABSTRACT

We present multi-epoch, total intensity, high-resolution images of 43GHz, $v=1$, $J=1-0$ SiO maser emission toward the Mira variable R Cas. In total we have 23 epochs of data for R Cas at approximate monthly intervals over an optical pulsation phase range of $\phi = 0.158$ to $\phi = 1.78$. These maps show a ring-like distribution of the maser features in a shell, which is assumed to be centred on the star at a radius of $1.6 \rightarrow 2.3$ times the radius of star, R_* . It is clear from these images that the maser emission is significantly extended around the star. At some epochs a faint outer arc can be seen at $2.2 R_*$. The intensity of the emission waxes and wanes during the stellar phase. Some maser features are seen infalling as well as outflowing. We have made initial comparisons of our data with models by Gray et. al. (2009).

Key words: maser – techniques: interferometric – star: AGB stars and post-AGB – star: individual: R Cas .

1 INTRODUCTION

The Asymptotic Giant Branch (AGB) is the last evolutionary stage of low- and intermediate-mass stars that are nuclear powered. This phase of evolution is characterised by nuclear burning of hydrogen and helium in thin shells above the electron degenerate core of carbon and oxygen. These stars are very large ($R \sim 1$ AU), very cool (2000-3000 K) and have abundant, molecular, dusty winds (mass loss rate $10^{-7} - 10^{-5} M_{\odot} \text{ yr}^{-1}$ (Herwig 2005).

Any AGB star in the end will lose mass in the form of a slow wind at a rate that will significantly affect the mass of the star. This produces a circumstellar envelope of escaping dust and gas particles. When the envelope becomes separated from the star, the mass-loss sometimes ceases in a short period of time and the temperature drops as the wind flows away from the star, from about 3130 K at the photosphere to ≈ 740 K at $5.5R_*$ (Gray et. al. 2009); cooling takes place by line radiation from various molecules, especially H_2O . Some molecular species are formed in an equilibrium process deep in the atmosphere and are destroyed in the outer parts of the outflow by interstellar ultraviolet radiation (H_2 , CO, H_2O). Other species, for example SiO, are depleted due to condensation on dust particles at a few stellar radii (Habing 1996). The observations show that almost all AGB stars are pulsating variables, the pulsations produce waves which steepen up into shock waves in the large density gradient of the stellar atmosphere. These pulsational shocks are well-known to influence the dust formation zone (Freytag et. al. 2008). Stellar pulsations cause waves which

travel into the thinner outer layers of the atmosphere and develop into shocks with temperature and density variations strong enough to trigger intermittent dust formation. Large opacities allow the dust grains to capture the stellar radiation efficiently, leading to an outward acceleration of the dust particles which is transmitted to the gas by collisions, causing a slow but dense outflow from the star. The mass loss controls the termination of the AGB phase. When the envelope becomes optically thin, the star leaves the AGB phase (Lattanzio et. al 1998). Shock waves can produce the necessary physical condition (SiO abundance, kinetic temperature and density) for collisional pumping of SiO maser (Elitzur et. al 1980). Their positions is also consistent with that of optically thick molecular layers responsible for radiative pumping of these masers (Gray et. al. 2009).

The gas in the circumstellar envelope is largely molecular with a composition that reflects the stellar chemistry. The molecules are located in different parts in the envelope in shells of different radii and widths, depending on the formation process and their resistance to shocks and ultraviolet photons (Olofsson 1999).

The gas outflow of AGB star is normally considered to be spherically symmetric. Asymmetric structures are observed in AGB stars, for example in the radio photospheres of Mira, W Hya and R Leo (Reid & Menten 2007) and in optical photosphere (Karovska 1997).

R Cassiopeia is an oxygen-rich AGB star which is classified as an M-type Mira-variable. Its optical brightness varies from magnitude +4.7 to +13.5 with a period of 430 days and

its mass is about $1.2 M_{\odot}$. Vlemmings et al. (2003) used astrometric VLBI to measure a distance of 176_{-45}^{+92} pc with a proper motion of $(85.5 \pm 0.8, 17.5 \pm 0.7)$ mas yr $^{-1}$ in R. A. and Dec., respectively. Various estimates of the stellar velocity V_{\star} appear in the literature; we tabulate these in Table A1 and adopt the mean value, $+24$ km s $^{-1}$, standard deviation 2 km s $^{-1}$.

Because the maser emission is so bright, it allows the inner circumstellar envelope to be resolved on sub-milliarcsecond scales. The SiO masers are found in a region close to the star, within the dust formation zone, located at a radius of about 2 to 4 stellar radius (R_{\star}). They are observed as clumpy, partial rings centred on the star; the masers fit a model of a hollow, expanding ellipsoid as observed in TX Cam and U Her. The masing action needs a long path through a relatively constant tangential velocity to produce the necessary gain to be visible, this condition is often met for a line tangent to the masing region with low turbulence because the turbulence would reduce the path length at a given velocity limiting the gain and hence the brightness (Diamond et. al. 1994).

The H $_2$ O maser is located in the inner parts of the circumstellar shell between ≈ 10 to $20 R_{\star}$ where the temperature ranges from 300 K to 1000 K and densities are $10^7 - 10^9$ cm $^{-3}$ (Benson & Little-Marenin 1996). The OH masers are found in the region furthest from the star as described by Cohen (1989).

2 OBSERVATIONS AND DATA REDUCTION

The SiO masers around R Cas were observed as part of a more extensive programme of VLBA¹ monitoring of other stars. In total we have 23 epochs of data for R Cas. Data were recorded at each VLBA antenna in dual-circular polarization in two 4 MHz windows, each digitally sampled at the full Nyquist rate of 8 Mbps in 1-bit quantization. The lower spectral window was centred at a fixed frequency corresponding to the $v=1, J=1-0$ SiO transition, at an assumed rest frequency of 43.12207 GHz and a systemic velocity $V_{\text{LSR}} = +24$ km s $^{-1}$. R Cas was observed for three 45-minute periods evenly spread over the 8 hour duration of the run. Adjacent to each R Cas observation, 5 minutes was spent observing the continuum calibrator 0359+509 at the same frequency as R Cas. The data were correlated at the VLBA correlator in Socorro, NM. The correlator accumulation interval was set to 2.88 seconds. All polarization correlation products (RR, RL, LR, LL) were formed. This configuration produced auto- and cross-power spectra in each 4 MHz baseband with a nominal velocity spacing of ~ 0.2 km.s $^{-1}$. Table 1 shows the epoch code, the date of observation and the corresponding optical phase.

We reduced the data using the standard approach to VLBI spectroscopy within the NRAO AIPS package (<http://www.aips.nrao.edu/cook.html>). We processed the visibility data using the semi-automated spectral-line polarization calibration pipeline described

by Kembell et. al. (1995) and further developed by Kembell & Diamond (1997). We summarise the main steps here. We started by editing the data. We derived corrections for the phase-rate and the delay using the point-like calibration source 0359+509. The Kitt Peak (KP) antenna has good stability in both pointing and receiver gain so we used it as the reference antenna for all relevant stages at all epochs. We also scaled the KP autocorrelation spectra for 0359+509 with respect to the system temperature in order to derive the amplitude scale for all cross-power data (see Kembell et. al (2009) for details). We also used 0359+509 to correct for the phase response across the bandpass. We applied the delay, rate, amplitude and bandpass calibration to R Cas.

At each epoch, we selected a reference group of strong channels from R Cas and derived the residual rate corrections and then phase and amplitude corrections, which were applied to all channels. We took care to preserve the low Stokes V signature during amplitude calibration. We also corrected for parallactic angle rotation. Additional polarization calibration and results will be presented in a separate paper. After all calibration, we produced image cubes for R Cas at each epoch. We imaged 56 channels around the peak, each 0.217 km.s $^{-1}$ wide, image size 102.4×102.4 or 204.8×204.8 mas, in order to enclose a greater extent than any expected emission. The naturally-weighted restoring beam varied from epoch to epoch by a few mas and by a few degrees in position angle, but the close similarities show that the visibility plane coverage was consistent. The average beam size was $(0.039 \pm 0.007) \times (0.020 \pm 0.008)$ mas² at average position angle $(39 \pm 17)^{\circ}$. The thermal noise σ_{rms} in quiet channels was 30 mJy beam $^{-1}$.

We used the AIPS task SAD to fit 2-dimensional Gaussian components to each clump of emission brighter than $5\sigma_{\text{rms}}$ in each channel, using the method of Gonidakis et. al. (2010). We grouped components if their position in adjacent channels agreed within a beamwidth ~ 1 mas, rejecting isolated components. We term these groups ‘features’ and we found the error-weighted mean position and flux-weighted mean velocity of each feature. Since there was no external phase-referencing, all positions were initially obtained relative to the brightest component at each epoch. We aligned the emission at different epochs following the method described by Cotton et. al. (2004). For each candidate position we found the flux-weighted mean radius of all SiO maser components and then the inner and outer radii which enclosed 90 percent of the total emission. The centre of expansion is defined as the position giving the narrowest ring enclosing 90 percent of the emission. We then inspected the changes in component distribution relative to each centre. Some series of components formed very distinctive patterns which could be used to trace the emission from one epoch to the next. In most cases, alignment using the fitted centres of expansion gave very small and approximately symmetric shifts. However, at some epochs the maser distribution was very lop-sided, the shells were very poorly defined and we adjusted the apparent centres by eye to minimize the position changes of distinctive features. The estimated radii are given in Table 2. We estimated the errors arising from:

- (a) Signal-to-noise ratio based fitting errors from SAD;
- (b) Difference between finding the centre by eye and the automated fitting.

¹ The VLBA (Very Long Baseline Array) is operated by the the National Radio Astronomy Observatory, a facility of the National Science Foundation operated under a cooperative agreement by Associated Universities, Inc.

Epoch Code	Observing Date	Optical Phase ϕ
BD62A	1999-Sep-09	0.158
BD62B	1999-Oct-15	0.241
BD62C	1999-Nov-14	0.310
BD62D	1999-Dec-19	0.390
BD62E	2000-Jan-15	0.452
BD62F	2000-Feb-14	0.521
BD62G	2000-Mar-17	0.595
BD62H	2000-Apr-21	0.675
BD62I	2000-May-21	0.744
BD69A	2000-Jun-22	0.818
BD69B	2000-Jul-16	0.873
BD69C	2000-Aug-21	0.956
BD69D	2000-Sep-21	1.027
BD69E	2000-Oct-19	1.091
BD69F	2000-Nov-17	1.158
BD69G	2000-Dec-20	1.234
BD69H	2001-Jan-20	1.305
BD69I	2001-Feb-19	1.374
BD69J	2001-Mar-16	1.432
BD69K	2001-Apr-15	1.501
BD69L	2001-May-19	1.579
BD69M	2001-Jun-24	1.662
BD69N	2001-Aug-16	1.783

Table 1. Observing dates and epochs.

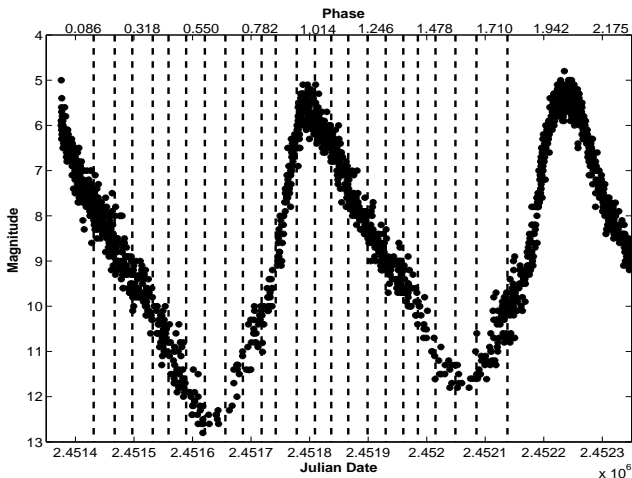


Figure 1. The light curve of R Cas provided by the AAVSO. The dashed vertical lines indicate the dates of our observations.

3 RESULTS

The optical light curve of R Cas provided by the AAVSO², is shown in Fig. 1. The dashed lines indicate the VLBA observational epochs that span the time interval from 1999 September 09 to 2001 August 16, corresponding to an optical phase interval of $\phi = 0.158$ to $\phi = 1.783$. Fig. 2 shows the flux density in Jansky of SiO maser emission toward R

² We acknowledge with thanks the variable star observations from the AAVSO (American Association of Variable Star Observers) International Database contributed by observers worldwide and used in this research.

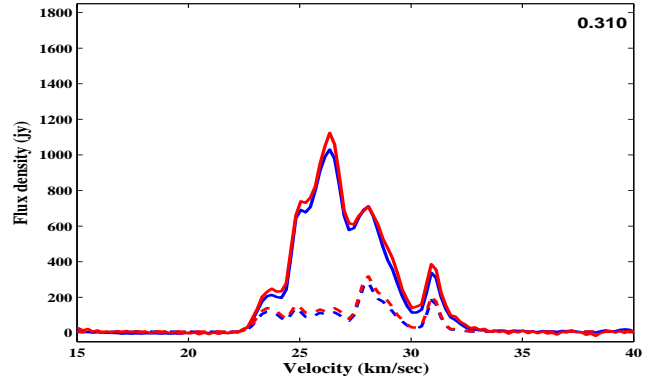


Figure 2. The flux density detected by the KP antenna (solid line) and by the shortest baseline (LA – PT) (dashed line), for the two hands of polarization (red=right-hand, blue=left-hand).

Epoch	Radius (mas)	error (mas)
BD62A	25.46	0.67
BD62B	27.09	0.05
BD62C	27.08	1.77
BD62D	26.05	1.22
BD62E	27.10	1.59
BD62F	28.43	1.98
BD62G	27.41	2.11
BD62H	28.09	0.3
BD62I	28.49	0.53
BD69A	27.29	1.64
BD69B	27.71	0.37
BD69C	28.00	1.5
BD69D	27.98	0.16
BD69E	27.50	0.5
BD69F	28.15	1.71
BD69G	28.52	2.5
BD69H	29.16	0.26
BD69I	27.15	0.17
BD69J	26.83	0.63
BD69K	25.11	3.11
BD69L	23.96	1.22
BD69M	25.87	3.83
BD69N	26.82	1.68

Table 2. Estimated radii of the SiO maser shell at each epoch.

Cas in both RR and LL polarizations. In this figure, the solid line indicates the single-dish flux density for the Kitt Peak antenna, and the dashed line, the flux density for the shortest VLBA baseline PT-LA. It clear from the figure that the shortest baseline of the VLBA detected about 27 percent of the single dish SiO flux. Comparisons for all epochs are shown in Figs. B1 – B3.

The gross morphology of the SiO maser emission toward R Cas in each individual epoch is shown in Fig. 3 and Fig. 4. Predominantly, the maser emission is confined to a narrow projected ring in phases $\phi = 0.241 - 1.374$. The first epoch, $\phi = 0.158$, shows an additional, outer arc; a few outlying masers are also seen at $\phi = 0.744 - 0.873$. From $\phi = 1.432 - 1.783$, the maser emission has an irregular shape, and the maser spots are very faint. The shell is dominated by an

Eastern arc during the first stellar period and by a Western arc during the second period. Fig. 5 shows the SiO maser features for all 23 epochs, superimposed on one plot. This shows that the SiO emission is predominantly situated in a ring that is poorly filled at the north and south. This ring has a radius of $1.6 - 2R_*$ depending on the observing epoch.

Fig. 6 shows the observed ring radii (tabulated in Table. 2) plotted as a function of stellar phase. The error bars on the points indicate the ring thickness, computed as the standard deviation in the observed ring radius. We fitted a parabolic function (solid line) to the data in Fig. 6 that shows the increase in the ring diameter over the phase range $\phi \sim 0.1$ to $\phi \sim 1.3$ (Diamond & Kemball 2003). The projected shell starts shrinking beyond the optical phase ~ 1.3 .

4 DISCUSSION

4.1 Morphology

The ring-like appearance of the SiO masers (Fig. 5) is thought to arise from a spherical shell, wherein strong radial acceleration or deceleration causes predominantly tangential amplification. The remnant of an outer, presumably older, shell is seen in the East in Fig. 3 ($\phi = 0.158$) and Fig. 4. At this first epoch and at $\phi \geq 1.234$, some faint emission is seen within 20 mas of the centre of expansion. This could be due to the emergence of a new shell and, indeed, the shell radius shrinks at $\phi \geq 1.374$ (discussed further in Section 4.3). Alternatively, the central masers could be radially beamed from parcels of gas temporarily moving at a fairly steady velocity, in between acceleration and deceleration. Most of the inner masers are red-shifted, suggesting infall, since they lie along the line of sight to the star, which would be optically thick to maser emission from the back of the shell.

4.2 Maser shell asymmetry

Figs. 3 and 4 show that the SiO emission is dominated by an Eastern arc during the first stellar cycle, whilst the Western side of the shell dominates for the remaining epochs. More than 3/4 of the emission comes from the East at $\phi = 0.158 - 0.744$ and more than 3/4 comes from the West at $\phi = 1.091 - 1.783$ as it is seen in Fig. 7. A similar dominance by one (Western) arc was seen by Phillips et al. (2001) in two epochs of observation of the 86-GHz SiO masers in 1998. There are several possible explanations.

Firstly, if conditions in one hemisphere of a spherical SiO maser shell are more favourable for masing, the change in E-W asymmetry from phase to phase could be due to bulk rotation, away from us in the E and towards us in the W, about an N-S axis. This would require an equatorial velocity of 10–20 km.s⁻¹ which is about twice the observed line of sight velocities, but this could be due to turbulence and selective maser amplification in our direction. However, it is hard to conceive a physical mechanism for spherical solid-body rotation, although a flared disc might be possible.

Secondly, the star may eject mass into arcs, as has been seen in IRC+10216 (Murakawa et. al. 2005), which could mean that at some cycles, mass ejections were concentrated along the line of sight. In such cases we would see little or no SiO maser emission.

Thirdly, stellar activity may disrupt masing close to the star. Rudnitskij (2008) report that R Cas is known to display H α flares at intervals of several years (also seen from other Miras). This is the most probable explanation although the second factor could play a part.

4.3 Maser shell diameter

Fig. 6 shows the variation of the ring diameter for 23 epochs as a function of stellar phase. It is evident that expansion is the dominant overall kinematic behaviour between optical phases $\phi \sim 0.158$ to $\phi \sim 1.3$. Thereafter, the diameter decreases until a phase of $\phi \sim 1.58$. This may be due to the disappearance of outer maser features and/or infall under the influence of gravity. At $\phi > 1.58$ the diameter increases again, suggesting the impact of a new stellar pulsation. Similar behaviour was seen in TX Cam (Diamond & Kemball 2003).

We found the gravitational acceleration (g_{SiO}) was $\sim 3.27 \times 10^{-7}$ km s⁻² at the midpoint of SiO maser region (~ 26.56 mas) for a star mass of 1.2 M $_{\odot}$. By adopting a distance to R Cas of 176 pc (Vlemmings et al. 2003), we found that the required infall time for a parcel of gas across a maser zone of size ~ 12 mas is ~ 500 days. This estimate has an uncertainty of > 20 percent, mainly due to the uncertainty in the distance to R Cas, but is comparable to, or greater than, the stellar pulsation period of 431 days. Diamond & Kemball (2003) found a similar relationship for TX Cam. We also used our estimate of g_{SiO} to calculate that, if a parcel of gas was stationary at $\phi = 1.308$, it would attain a velocity of 14 km s⁻¹ at $\phi = 1.579$, which is almost equal to the velocity of 13.7 km s⁻¹ required to reach the observed minimum radius.

These results indicate that complex kinematics exist in the SiO maser region. The gas is subject to two main forces; outward pressure due to stellar pulsations and the inward force of gravity. Fig. 6 shows that expansion appears to be a slower process than infall over the same distance, consistent with a variable outward force but a more constant inward force. When the stellar pulsation pressure is weakest, at the outer edge of the SiO maser shell, the parcel of gas would start to fall back towards the star under its gravitational pull. If the parcel does not reach the inner edge of the shell before the next pulsation, it will then be pushed out further. These results, like those for TX Cam, are a step towards quantitative verification of pulsation models like Bowen (1988).

4.4 Maser models

We make some simple comparisons between the observed maser structure and the model of Gray et. al. (2009); a more detailed analysis will be presented in a future paper. The model deals with tangentially beamed emission, but although emission is seen along the line of sight to the star at some epochs, this is too faint to influence comparison of the models with the average velocity profiles or radii. This model predicts that the diameter of the maser ring should be about twice the size of the stellar photosphere. The optical stellar diameter of R Cas is 25.3 ± 3.3 mas at $\phi = 0.93$ (Weigelt et.al. 2000). We found that the SiO maser mean angular diameter, averaged over 23 epochs, is ~ 54 mas which

is double the photospheric diameter within the uncertainties, showing that the model is consistent with our data.

This model also predicts that the ring size increases from stellar phase 0.1 to 0.25 and then decreases. Fig. 6 shows that, during the first cycle, the radius continues increasing past phase 0.25. However, in the second cycle, the radius decreases sharply at the predicted phase. The model predicts that the maser weakens between phases 0.25 and 0.4. Fig. 8 shows that the flux density peaks at $\phi \sim 0.2$ and then decreases over the same phase range which suggests good consistency between our observations and the model.

Another prediction of the model is that the average velocity of the transition studied here moves to higher, red-shifted velocities, from phase 0.1 to 0.4. We tested this using the single dish (autocorrelation) observations shown in Figs. B1 – B3, in order to ensure that the full spectra were measured. The red and blue, dashed lines in Fig. 9 show the velocity structure averaged over this range of phase for the first and second cycles, respectively. The black vertical line indicates the stellar velocity (with an uncertainty of 2 km s^{-1}). The blue vertical line marks the flux weighted mean velocity for all epochs. The black, solid line is the model. This figure shows that the peak flux density is red-shifted in both the present R Cas data for the first cycle and in the model. The separation in the velocities of the peaks in the model and R Cas spectra is just 1.25 standard deviation in the R Cas data. The second cycle is not consistent with the model.

Fig. 10 shows that the SiO maser variability in R Cas has approximately the same period as its optical light curve with a phase lag ≈ 0.153 (66 days) which is consistent with the predictions of Pardo et. al. (2004).

At this point, we compare the observational data of R Cas with a computational model of an AGB star. This model combines hydrodynamic solutions with a maser radiative transfer code as described in Gray et. al. (2009), apart from the exceptions discussed below.

The Gray et. al. (2009) model was extended to sample 12 stellar phases between $\phi = 0.4$ to $\phi = 1.5$, so that the model pulsation passes through an optical maximum. We note that the model star is not specifically designed to represent R Cas. In Gray et. al. (2009), the 4 phase samples were modelled as separate snapshots, unrelated to each other in the sense of positional evolution of the masing objects. By contrast, the current model evolves the maser distribution by taking the output conditions of one sample as the input conditions for the next, as in Humphreys et. al. (2002). Therefore the maser spots have random positions only for the first sample (at phase 0.4 in the first cycle). We computed the inner, outer and mean radius for each model epoch, defined in the same way as for the observational data. The mean radius of the maser shell is plotted for R Cas, in Fig. 11. It is evident that the model maser shell is substantially smaller than R Cas. However, a significant decrease in mean radius is apparent following optical maximum in both model and R Cas. This is the most statistically significant radius change in the observational data. This shrinkage is delayed in the R Cas data, with respect to the model, by about 0.2 stellar periods. On inspection of the model spectra during the radius drop, the peak of the model 43-GHz spectrum shifts to the red by $\sim 7 \text{ km.s}^{-1}$.

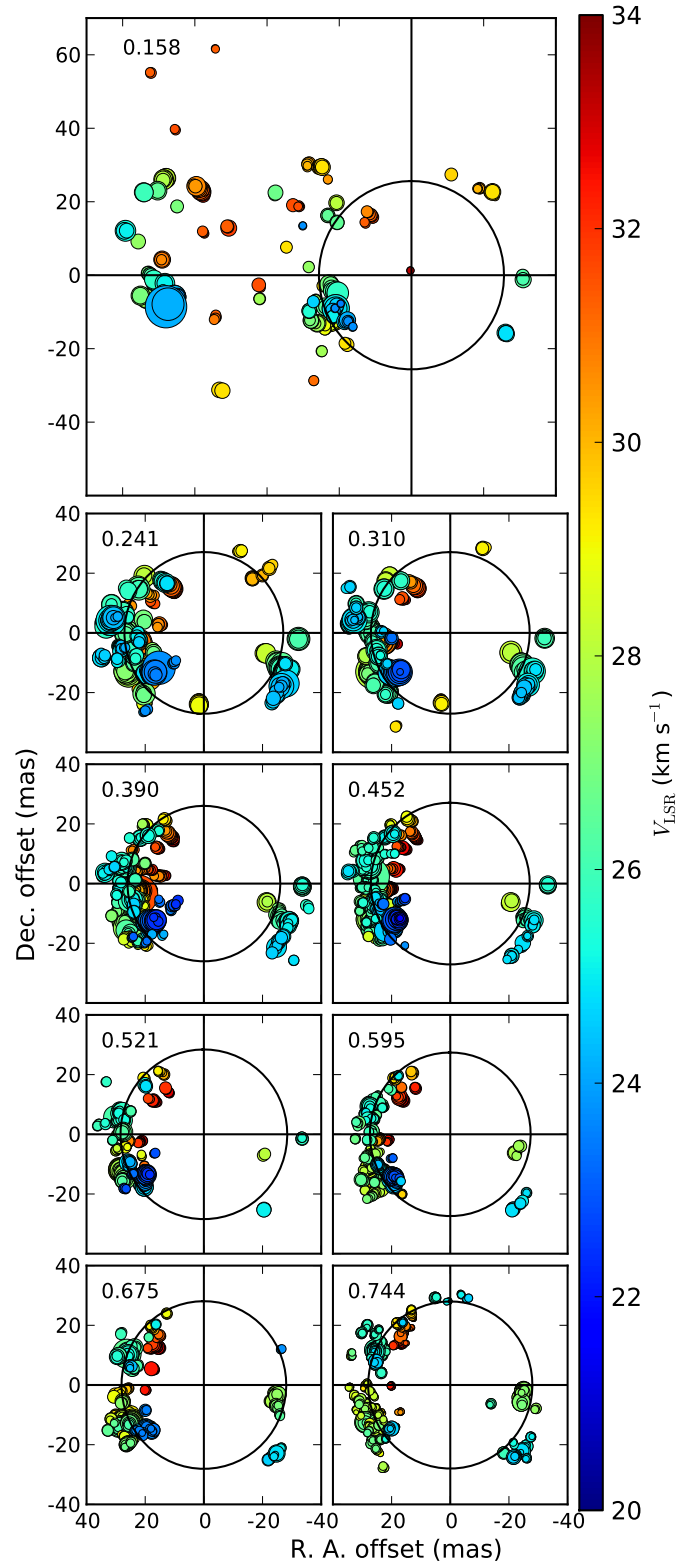


Figure 3. Total intensity images [Epochs (1-9)]. The symbol size is proportional to the square root of the flux density of each component, the large circles represent the mean maser shell.

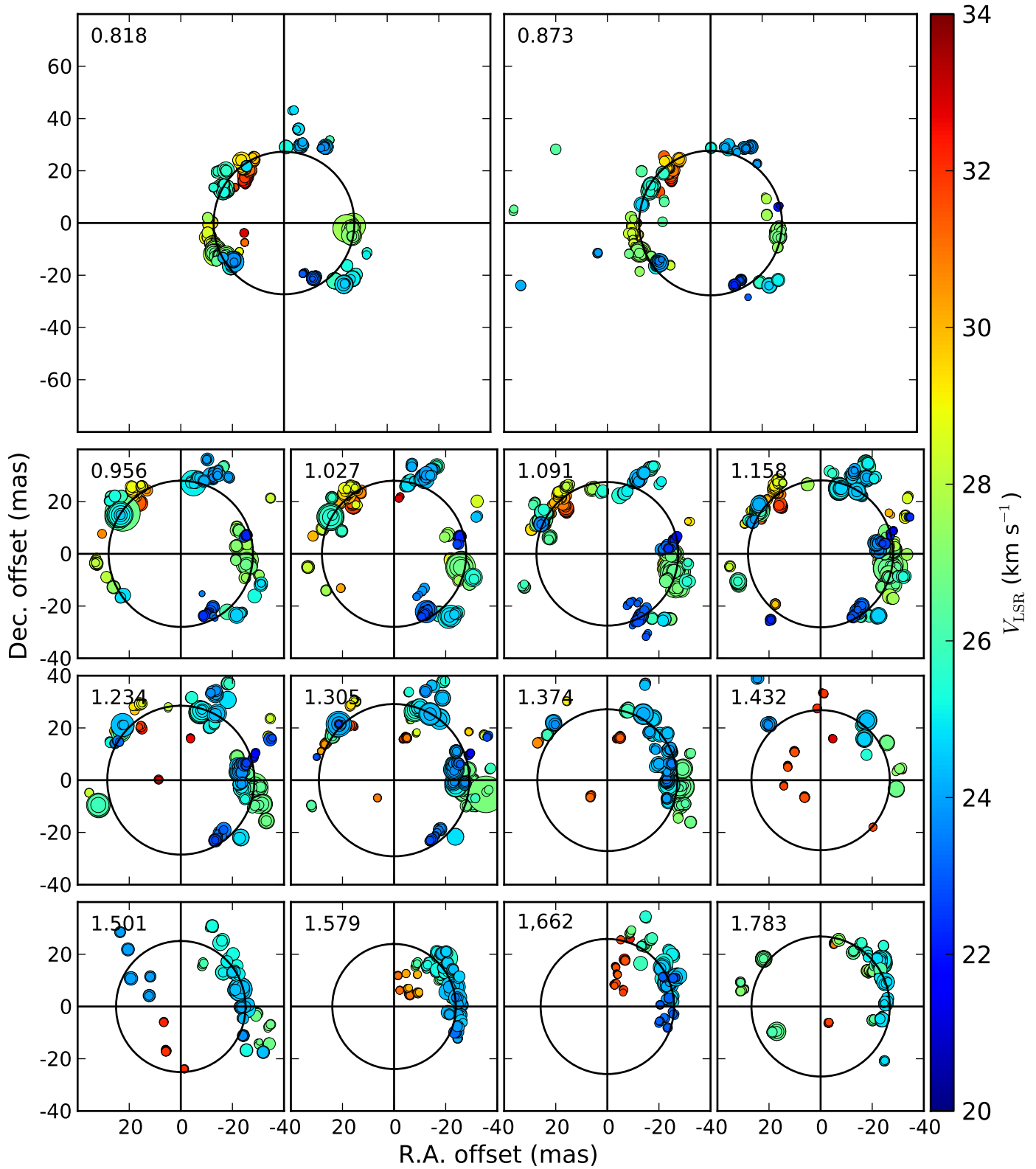


Figure 4. Same as Fig. 3 [Epochs (10-23)].

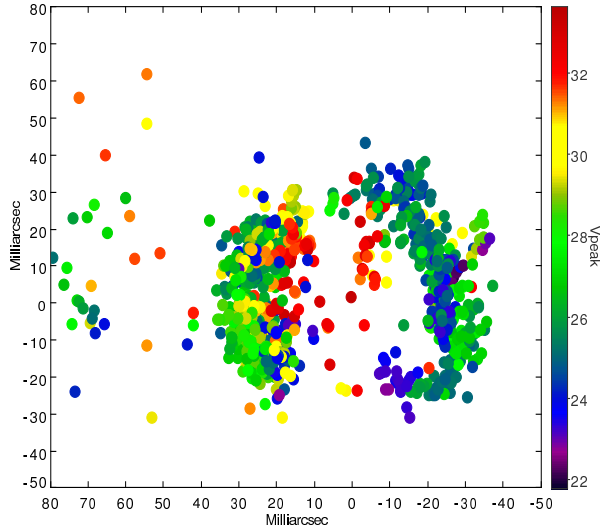


Figure 5. SiO maser features observed at all 23 epochs.

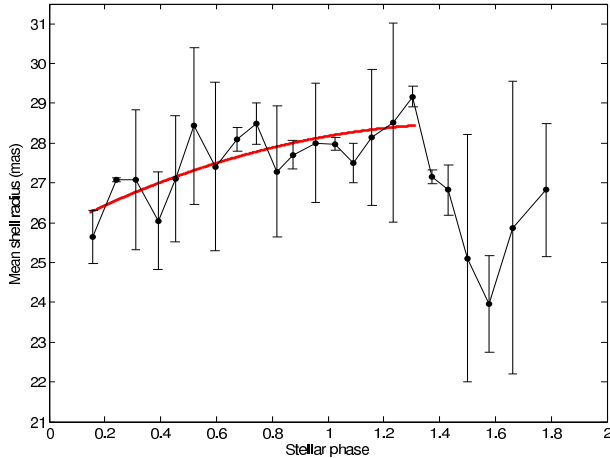


Figure 6. The variation of the SiO maser ring radius with the stellar phase.

This is consistent with the observed reddening of the R Cas emission during its contraction. We also inspected the model velocity at mean radius \bar{R} , and noted that the velocity was closer to infall at the \bar{R} during ring contraction than at optical maximum.

5 CONCLUSIONS

The SiO maser morphology in R Cas for the transition $v = 1, J=1 \rightarrow 0$ is described as a rarely completed ring structure, and the ring is dominated by an Eastern arc in the first stellar period and by a Western arc in the second stellar period. The result are compared with a model produced by Gray et. al. (2009) which predicts most of observed features in our data. The infall time towards the star is greater than the pulsation period with a factor of ~ 1.2 . The maser light curve behavior is similar to the optical light curve but with phase lag of 66 days.

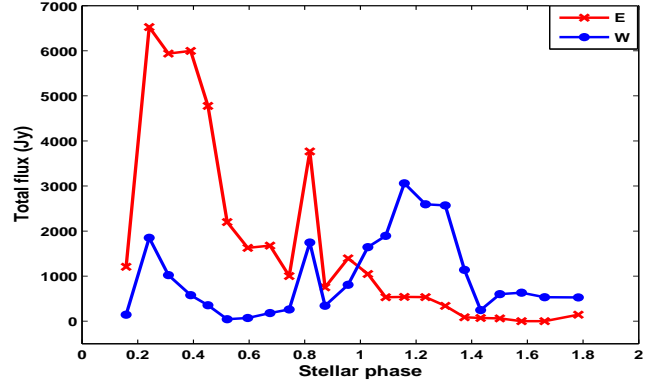


Figure 7. The total East- (Red) and West- (Blue) flux density for 23 epochs.

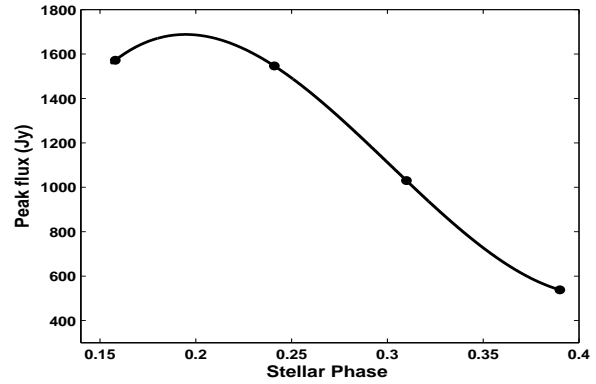


Figure 8. The peak SiO maser flux density as a function of the stellar phase over the interval described by the model of Gray et. al. (2009).

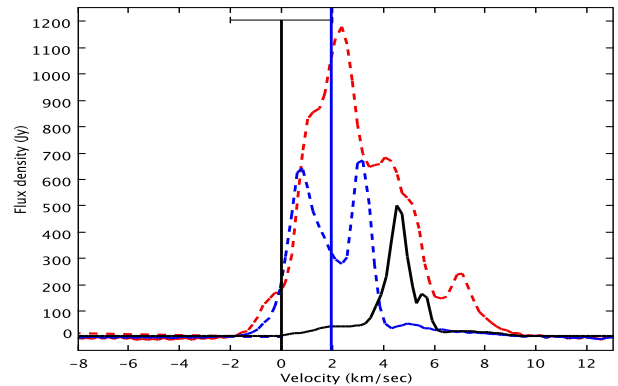


Figure 9. Total intensity SiO maser velocity profiles measured by a single dish. The red and blue dashed curves show the emission averaged over the first and second cycles, respectively. The black solid curve represents the model. The black vertical line is the stellar velocity with an uncertainty ($\pm 2 \text{ km.s}^{-1}$) and the blue vertical line is the flux-weighted mean velocity for all epochs.

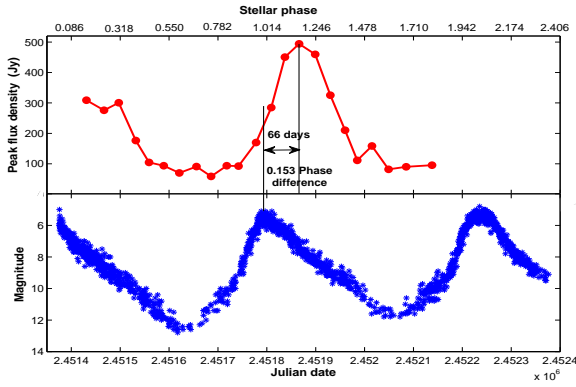


Figure 10. Phase difference between the maser light curve (upper frame) and the optical light curve (lower frame).

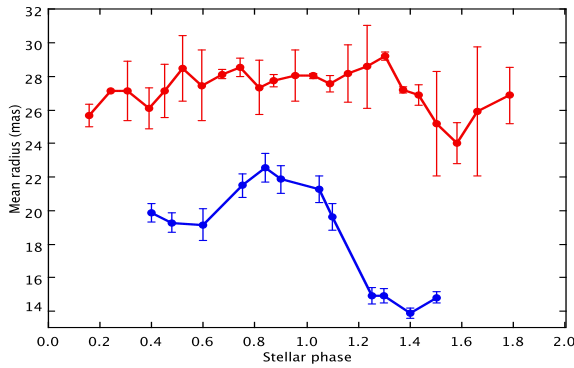


Figure 11. A comparison between the behaviour of the radius in the model (blue) and our data (red).

ACKNOWLEDGMENTS

Many thanks to VLBA for providing the data used in this paper and many thanks to AAVSO for providing the the optical light curve. The authors acknowledge the use of the UCL Legion High Performance Computing Facility, and associated support services, in the completion of this work. K.A.A. would like to extend his thanks to the Iraqi government for giving him the opportunity to do the PhD study at the University of Manchester and he thanks his friend Qusay Al-Zamil for some helpful suggestions that improved the presentation of the paper. We would like to extend our thanks to the referee for his helpful suggestions.

REFERENCES

- Benson, P. J., & Little-Marenin, I. R. 1996, *ApJS*, 106, 579
 Boboltz D. A. and Claussen M. J., 2004, *Astrophys. Jour.*, 608, 480
 Bowen, G. H. 1988, *ApJ*, 329, 299
 Cohen R. J., 1989, *Rep. Prog. Phys.*, 52, 881
 Colomer F., Reid M. J., Menten K. M. and Bujarrabal V., 2000, *Astron. Astrophys.* 355, 979
 Cotton W. D., Mennesson B., Diamond P. J., Perrin G., Coudé du Foresto V., Changnon G., van Langevelde H. J., Ridgway S., Waters R., Vlemmings W., Morel S., Traub W., Carleton N. and Lacasse M., 2004, *A&A*, 414, 275

- Diamond, P. J.; Kemball, A. J.; Junor, W.; Zensus, A.; Benson, J.; & Dhawan, V. 1994, *ApJ*, 430, 61
 Diamond, P. J. and Kemball, A. J., 2003, *Astrophys. Jour.*, 599, 1372
 Elitzur M. and Watson W. D., 1980, *Astrophys. Jour.* 236, 172
 Freytag, B. and Höfner, S., 2008, *A&A*, 483, 571
 Gray M. D., Wittkowski, M., Scholz, M., Humphreys, E. M. L., Ohnaka K. and Boboltz, D., 2009, *Mon. Not. R. Astron. Soc.*, 394, 51.
 Gonidakis I., Diamond P. J. and Kemball A. J., 2010, *Mon. Not. R. Astron. Soc.*, 406, 395.
 Habing H. J., *Circumstellar envelopes and Asymptotic Giant Branch stars*, *A&A Rev.*, 7:97-207, 1996. doi: 10.1007/PL00013287.
 Herwig F., 2005, *Annu. Rev. Astro. Astrophys.* 43, 435
 Humphreys, E. M. L., Gray, M. D., Yates, J. A., Field, D., Bowen, G. H. and Diamond, P. J., 2002, *A&A*, 386, 256H
 Jewell P. R., Snyder L. E., Walmsley C. M., Wilson T. L. and Gensheimer P. D., 1991, *A&A*, 242, 211.
 Karovska, M., 1997, *J. Am. Assoc. Var. Star Obs.*, 25, 75
 Kemball A. J., Diamond P. J. and Cotton W. D., 1995, *A&A*, 110, 383
 Kemball A. J., Diamond P. J., 1997, *ApJ*, 481, L111.
 Kemball A. J., Diamond P. J. Gonidakis I., Mitra M. Yim K., Pan K. and Chiang H., 2009, *ApJ.*, 698, 1721.
 Lattanzio, J. C. and Frost, C. A., 1998, *IUA, Symposium No. 189*, 373
 Matthews L. D. and Reid M. J., 2007, *Astrophys. Jour.* 133, 2291.
 Murakawa K., Suto H., Oya S. Yates J. A., Ueta T. & Meixner M., 2005, *A&A*, 436, 601
 Olofsson H., 1999, *I.A.U., Symposium No 191*, 3
 Pardo J. R., Alcolea J., Bujarrabal V., Colomer F., del Romero A. and de Vicente P., 2004, *A&A*, 424, 145.
 Phillips R. B., Sivakoff G. R., Lonsdale C. J., Doeleman S. S., 2001, *AJ*, 122, 2679
 Reid, M. J. & Menten, K. M., 2007, *Apj*, 671, 2068
 Rudnitskij, G. M. 2008, *Journal of Physical Studies*, 12, 1301
 Vlemmings W. H. T., van Langevelde H. J., Diamond P. J., Habing H. J. and Schilizzi R. T., 2003, *Astro. Astrophys.* 407, 213
 Weigelt G., Mourard, Denis, Abe Lyu, Beckmann, Udo, Chesneau, Olivier; Hillemanns, C, Hofmann, Karl-Heinz; Ragland, Sam D.; Schertl, Dieter; Scholz, Michael; 2000, *SPIE*, 4006, 617

APPENDIX A: ESTIMATES OF THE STELLAR VELOCITY

Various estimates of the stellar velocity V_* appear in the literature; we tabulate these in Table A1 and adopt the mean value, $+24 \text{ km s}^{-1}$, standard deviation 2 km s^{-1} .

V_{LSR} (km. s ⁻¹)	Reference
20.4	Jewell et. al. (1991)
24	Colomer et. al. (2000)
26	Vlemmings et al. (2003)
25.4	Boboltz et. al. (2004)
24.9	Matthews et. al. (2007)

Table A1. Stellar velocity.

APPENDIX B: PLOTS OF FLUX DENSITIES FROM A SINGLE DISH ANTENNA AND FROM THE SHORTEST BASELINE FOR DUAL-HAND POLARIZATION

Figs. B1, B2, B3 compare the flux density from a single dish Kitt Peak (KP) (solid line) and from the shortest baseline between Los Alamos and Pie Town (LA – PT) (dashed line) for the two hands of polarization (red = right hand, blue = left hand). The number on each plot indicates the stellar phase. The apparent offset between L and R is probably a residual error.

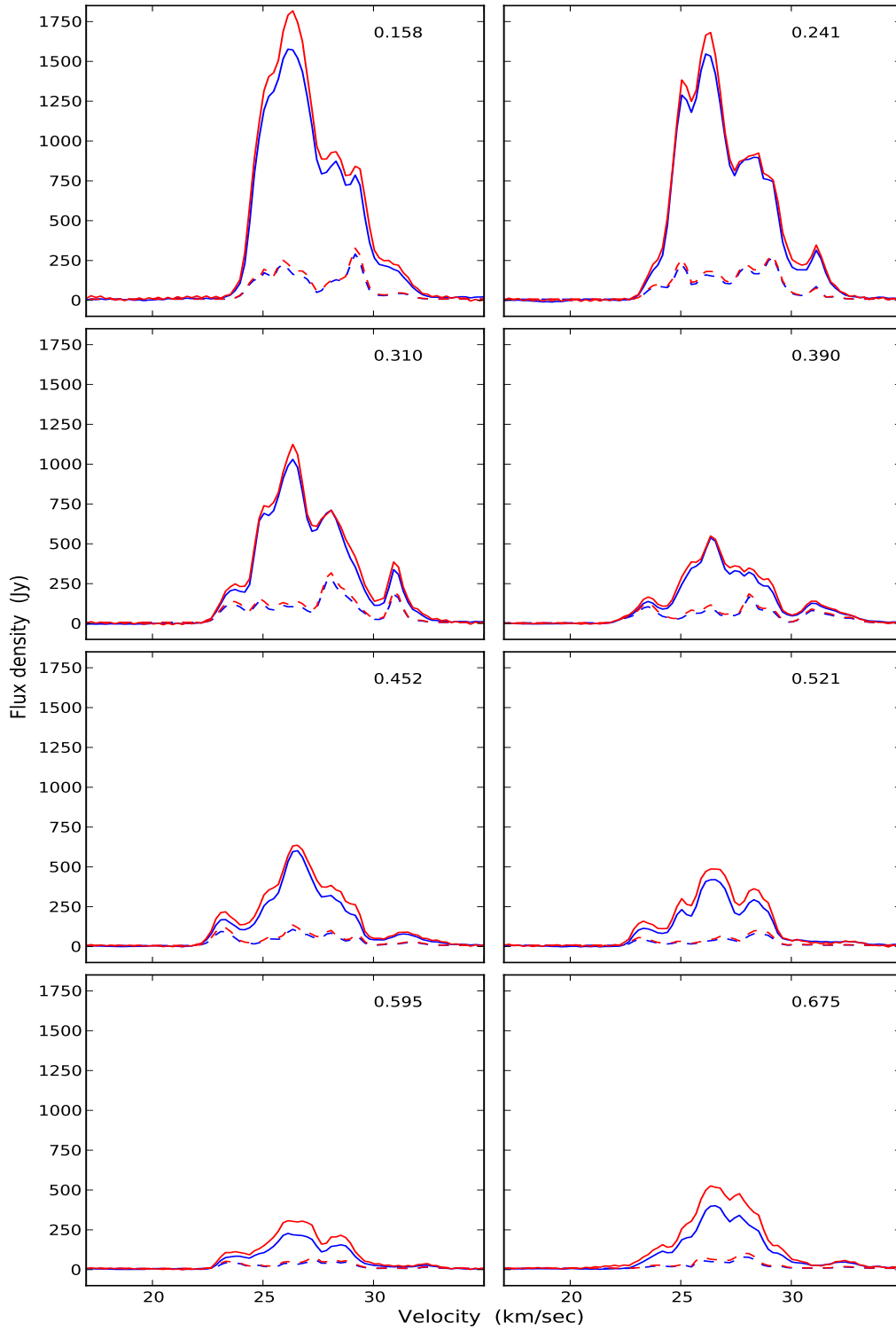


Figure B1. The flux density for antenna KP (solid line) and shortest baseline (LA - PT) (dashed line) for the two hands of polarization (red=right-hand, blue=left-hand) for epochs 1 - 8.

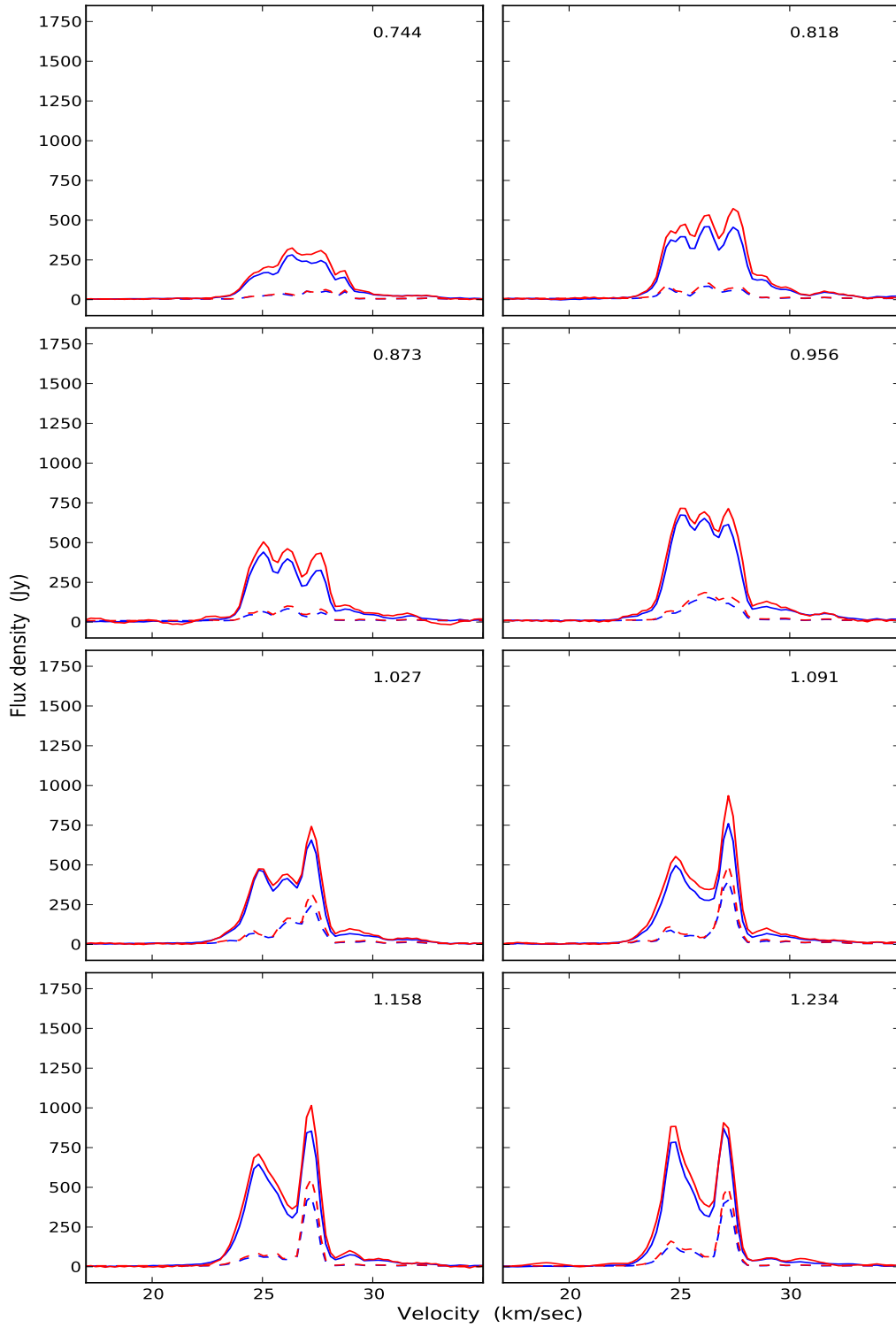


Figure B2. Same as Fig. B1 for epochs 9 –16.

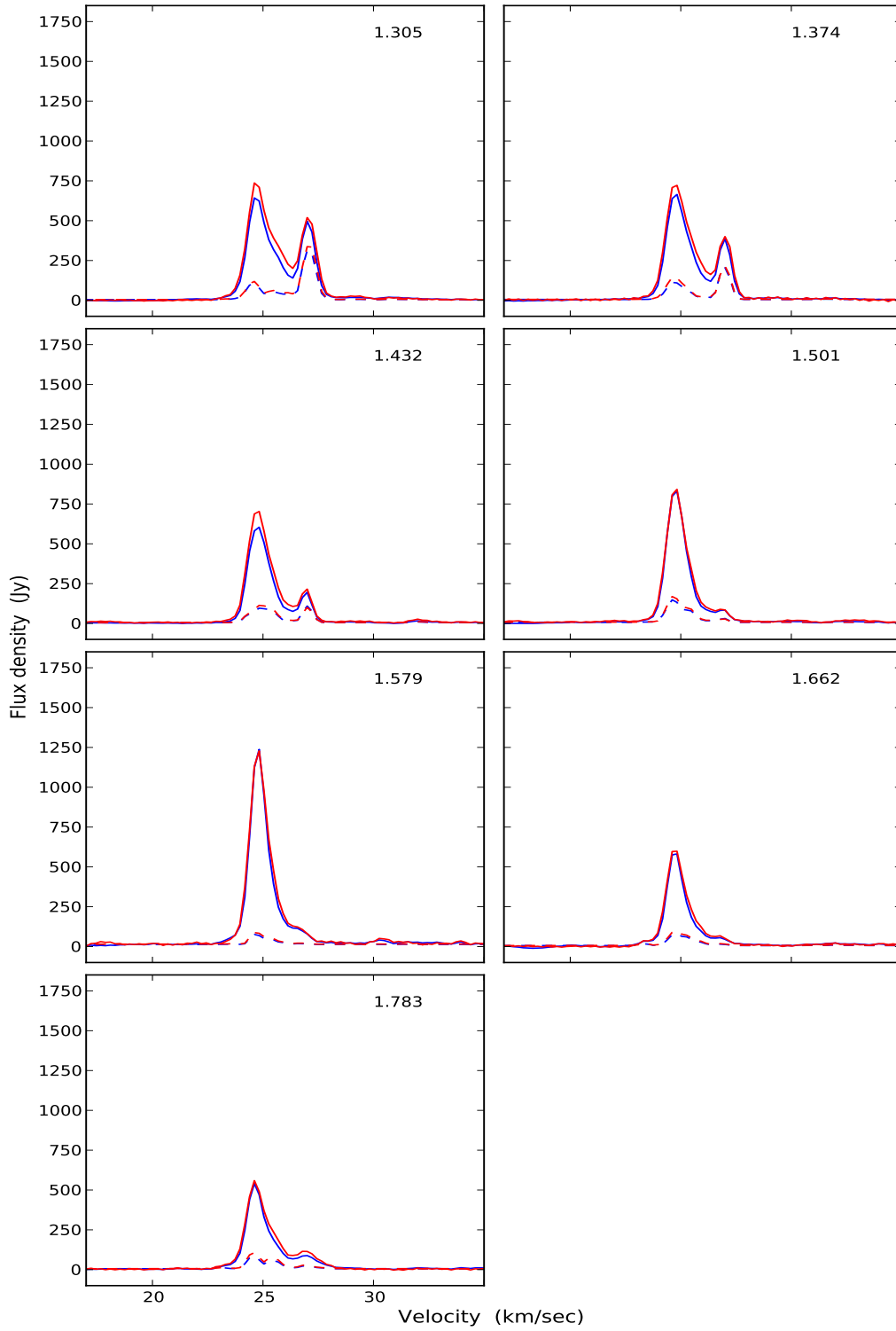


Figure B3. Same as Fig. B1 for epochs 17 – 23.